ROYAL SOCIETY
OF CHEMISTRY

PAPER

Check for updates

Hydrothermally synthesized poorly-crystalline binary oxides with ZrW$_2$O$_8$ composition: preparation, structural analysis, and catalytic activity for the alkylation of anisole with benzyl alcohol†

Takashi Yamamoto, [ID] *[ab] Seina Heiuchi,[b] Maki Kondo,[b] Kei Tabusadani[a] and Atsushi Sakaki [ID][c]

Hydrothermally synthesized poorly-crystalline metastable Zr–W binary hydroxide (W/Zr = 2), after calcination, was confirmed to be a strong solid acid catalyst to promote the alkylation of anisole with benzyl alcohol. The preparation conditions, structure of the as-prepared catalysts and the calcined hydroxides were investigated using XRD, nitrogen adsorption isotherms, TG-DTA, and XANES/EXAFS techniques. The crystalline phase was controlled by the hydrochloric acid concentration used for preparing a mother gel, and 5–9 M HCl was suitable for preparing the active phase. The tungsten species exists as a six-valent WO$_6$ distorted octahedron connected with the ZrO$_7$ unit *via* corner-sharing linkages. The incompleteness of the network structure is suggested to be responsible for the solid acidity.

1. Introduction

ZrW$_2$O$_8$ is a compound appearing in the phase diagram of the ZrO$_2$–WO$_3$ system[1] and is known as a negative thermal expansion material over a wide temperature range of 0.3–1050 K.[2–4] It is thermodynamically stable between 1378 and 1530 K, and its low-temperature synthesis is possible by calcination of ZrW$_2$O$_7$(OH)$_2$·2H$_2$O crystals at ∼873 K.[5] Generally, the highly crystalline ZrW$_2$O$_7$(OH)$_2$ phase[6] is synthesized during the hydrothermal treatment of a mother gel in acidic halide-containing media. The effects of HCl concentration used and/or the time of hydrothermal treatment on the crystalline phase have been examined.[7–11] We have confirmed that a poorly crystalline phase (tentatively denoted as ZWO-I) forms before forming the well-crystalized ZrW$_2$O$_7$(OH)$_2$·2H$_2$O phase during hydrothermal treatment; the phase is stable after calcination at 873 K (Fig. S1†).[12]

Tungsten–zirconium binary oxide catalysts developed by Hino and Arata,[13,14] so-called tungstated-zirconia (WO$_x$–ZrO$_2$), have attracted considerable attention because of their strong acidity comparable to 100% H$_2$SO$_4$ and properties such as promoting the skeletal isomerization of light alkanes under

mild conditions, easy preparation and handling, as well as high thermal stability of up to ∼1100 K.[15–18] Although the origin of the acidic property and the structure of acid sites have been examined by many research groups,[13,19–26] the problems remain unsolved to date. We presume that a mixed metal oxide forms at the interface between the loaded species and support, and a series of Zr–W binary oxides are candidates for a model catalyst, conventional tungstated-zirconia. Note that the W/Zr atomic ratio of conventional tungstated-zirconia (15 wt% as WO$_3$) is <0.1, whereas that of ZrW$_2$O$_8$ is 2.

We reported that the as-mentioned poorly crystalline ZWO-I phase acts as a solid acid to promote the alkylation of anisole with benzyl alcohol, whereas the amorphous silica-alumina of the typical strong solid acid, highly crystalline ZrW$_2$O$_8$ and ZrW$_2$O$_7$(OH)$_2$ are catalytically inert under the same reaction conditions.[12] In this study, we closely examine the ZWO-I phase preparation condition, structure, and catalytic performance. Although we recorded W L-edge XAFS of the ZWO-I phase in a previous study, we did not perform Zr K-edge XAFS characterization or curve-fitting analysis at the W L3 edge. In the current solid acid catalyst, the Zr edge EXAFS analysis is expected to provide information about the boundary structure between the tungsten and zirconium species. The XRD pattern identical to the ZWO-I phase has been reported by Xing *et al.*,[27] Ando *et al.*,[28] and Lucas *et al.*[29] Because of the wide lines in the powder X-ray diffraction patterns, the phase was identified as amorphous, and the precise structural characterization has not been performed. Ando *et al.* reported that the phase acts as a solid acid catalyst to promote the alkylation of anisole with

[a] Department of Science and Technology, Tokushima University, Tokushima 770-8506, Japan. E-mail: takashi-yamamoto.ias@tokushima-u.ac.jp

[b] Department of Mathematical and Material Sciences, Tokushima University, Tokushima 770-8502, Japan

[c] Nichia Corporation, Anan, Tokushima 774-8601, Japan

benzyl alcohol.[28] Because zirconium sulfate and sulfuric acid were used in their preparation, it is unknown whether sulfated zirconia[30,31] of a typical strong solid acid exists on the surface or not. To our knowledge, there have been no other studies reporting that the ZWO-I phase itself promotes the acid-catalyzed reaction and detailed characterization.

2. Experimental

2.1. Preparation

Zr–W binary oxide precursor was prepared *via* the hydrothermal treatment of a mother gel at 453 K based on previous studies.[12,27] In particular, 100 mL of the aqueous solution of 0.021 M $(NH_4)_6H_2W_{12}O_{40}$ (ammonium metatungstate, Wako Chemicals) was added to 50 mL of 0.25 M $ZrOCl_2$ (zirconium oxychloride, Nacalai, GR) at 333 K and stirred for 2 h. Then, 50 mL of 0–10 M hydrochloric acid (HCl) (Nacalai, GR) was added to the mixture and stirred for 5 h to prepare a mother gel. The mother gel was loaded into a Teflon bottle in an autoclave and statically heated at 453 K for 6–240 h. The white precipitate obtained was repeatedly washed with distilled water until Cl^- was free based on the $AgNO_3$ test. After drying at 383 K for 12 h, the as-synthesized binary hydroxide (ZWOH) was calcined at 673–1073 K for 3 h under air to form the corresponding binary oxide (ZWO). The samples prepared will be referred to hereafter as ZWOH_*X*M_*Y*h and ZWO_*X*M_*Y*h_*Z* where *X*, *Y*, and *Z* are the concentrations of the utilized HCl, time of hydrothermal treatment, and calcination temperature, respectively. Unless otherwise stated, the utilized HCl concentration, time of hydrothermal treatment, and calcination temperature were 6 M, 12 h, and 873 K, respectively.

The reference catalysts used were tungstated-zirconia[13,14] (home-made, reference JRC-WZ-1), sulfate-ion treated zirconium oxide (sulfated zirconia),[30] amorphous silica-alumina (JRC-SAL-4, 12.6 wt% as Al_2O_3), and hexagonal ordered mesoporous silica FSM-16.[32] Amorphous zirconium hydroxide $Zr(OH)_x$ was prepared by hydrolyzing a zirconium oxychloride aqueous solution at pH = 10 with an NH_3 aqueous solution, followed by aging, washing, and drying at 383 K. Conventional tungstated-zirconia was prepared by impregnation of the $(NH_4)_{10}H_2W_{12}O_{42}$ (ammonium para-tungstate, Nacalai, GR) aqueous solution on $Zr(OH)_x$ at 353 K and drying, followed by calcination at 1073 K for 3 h.[22] The loading amount was 15 wt% as WO_3. Sulfated zirconia was prepared by impregnation of 0.5 M H_2SO_4 on $Zr(OH)_x$ at room temperature for 0.5 h; it was filtered, followed by calcination at 873 K for 3 h. FSM-16 was synthesized using a water glass (Fuji Silysia Chemical; SiO_2: 25.3 wt%, Na_2O: 7.56 wt%, Al: 54 ppm, Fe: 3.6 ppm, Ti: 2.3 ppm, Ca: 5.7 ppm) and hexadecyltrimethylammonium bromide (Kishida Chemical). The preparation procedure of FSM-16 and the acidic properties have been previously reported in detail.[33–35] Monoclinic-ZrO_2 was prepared by calcination of $Zr(OH)_x$ at 1573 K. In_6WO_{12} was synthesized *via* a solid-state reaction by calcination of pelletized In_2O_3–WO_3 mixture at 1273 K.

2.2. Characterization

XRD patterns were recorded using a Miniflex diffractometer (Rigaku) equipped with a Ni-filtered Cu Kα radiation source.

The N_2 adsorption isotherms at 77 K were measured using a BELSORP-mini (MicrotracBEL). Each sample was outgassed for 2 h before measurement at 573 K (ZWO) or room temperature (as-synthesized ZWOH). The Dollimore–Heal method was used to analyze the adsorption data to obtain the pore size distribution. A simultaneous thermogravimetric and differential thermal analysis (TG-DTA) was performed under air using a DTG-60 analyzer (Shimadzu) at a heating rate of 10 K min^{-1}. The W L-edge X-ray absorption spectra were recorded using a laboratory-type spectrometer R-XAS Looper (Rigaku)[36] in the transmission mode at room temperature. A curved Si(620) or Si(400) monochromator crystal was used in W L1-edge XANES and W L3-edge EXAFS experiments, respectively. Zr K-edge X-ray absorption spectra were recorded at the BL16B2 at SPring-8 using a Si(311) double-crystal monochromator. For XANES analysis, the background removal followed by normalization was performed using Igor Pro 6 program.[37] The energy was not calibrated. The data reduction for the EXAFS analysis was performed using the REX2000 program.[38] Fourier transforms were applied to EXAFS in the *k*-ranges of ~3–11 Å^{-1} and 3–18 Å^{-1} at the W L3- and Zr K-edge, respectively. Because of the intrinsic contamination of Hf species in the used zirconium regent, the available *k*-range of W L3 edge EXAFS is limited to Hf L2-edge (10 739 eV). The FEFF8.4 program[39] was used to calculate the phase shift and backscattering amplitudes.

2.3. Catalysis

The alkylation of benzyl alcohol with anisole was performed using a stirred batch reactor under dry N_2 atmosphere typically at 393 K. Before the reaction, 100 mg of the catalyst was outgassed at 473 K for 2 h. The reactor was loaded with 0.64 mL of benzyl alcohol (6.2 mmol) and 10 mL of anisole (92 mmol). The product distributions were analyzed using a GC-14A gas chromatograph (Shimadzu) equipped with a flame ionization detector. *n*-Decane was used as an internal standard.

3. Results

3.1. Structural analysis

3.1.1. XRD. We reported that poorly crystalline catalytically active binary hydroxide (ZWO-I) was obtained by hydrothermal treatment of a mother gel for 12 h.[12] Although 6 M HCl was used to prepare the mother gel, the effect of HCl concentration on the obtained crystalline phase and catalytic performance was not examined. The dependence of HCl concentration on the crystalline phase was then investigated. Fig. 1 shows the XRD patterns of the as-prepared binary hydroxides and calcined binary hydroxides prepared with various HCl concentrations. The obtained products were classified based on crystalline phase formed controlled by the concentration as follows: Group A (10 M), Group B (5–9 M), Group C (2, 3 M), and Group D (0–1 M). The diffraction pattern of the as-prepared Group A (ZWOH_10M_12h) was identified as that of highly crystalline $ZrW_2O_7(OH)_2 \cdot 2H_2O$. It was transferred to cubic ZrW_2O_8 by calcination at 873 K as was the case in previous studies.[7,8,10] As-synthesized Groups B and C materials gave a set of broad
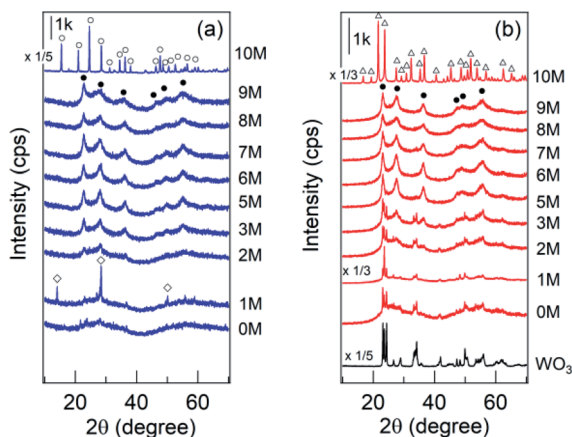
Fig. 1 XRD patterns of the hydrothermally synthesized (a) binary hydroxide ZWOHs prepared at various HCl concentrations and (b) ZWOs calcined at 873 K. Hydrothermal treatment: 453 K, 12 h. ○: $ZrW_2O_7(OH)_2 \cdot 2H_2O$, ●: ZWO-I, △: ZrW_2O_8, ◇: tungsten bronze.

diffraction lines in their XRD patterns, which has been confirmed.[12] We tentatively named the phase ZWO-I. Calcination at 873 K had no effect on these patterns in Group B; however, the formation of crystalline WO_3 coexisting with ZWO-I was detected in Group C. Diffraction lines suggested to be those of the tungsten bronze phase, presumably assigned to $(NH_4)_xWO_3$,[40–42] were observed overlapping with a broad amorphous halo in cases for the as-synthesized Group D materials. After calcination, a crystalline WO_3 phase was confirmed. In cases wherein the concentration of the utilized HCl for preparing a mother gel was less than 1 M, ZWO-I and/or $ZrW_2O_7(OH)_2$ single phases were not formed even after 72 h of hydrothermal treatment at 453 K (Fig. S2†).

3.1.2. Thermal analysis. Fig. 2 shows TG-DTA profiles of the typical as-synthesized ZWOHs. A gradual weight loss was
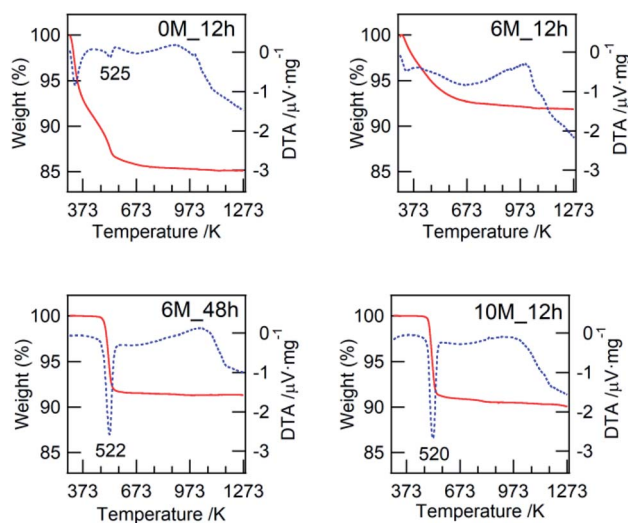

Fig. 2 TG-DTA profiles of the typical as-synthesized binary hydroxide prepared with different HCl concentrations and hydrothermal treatment times. Solid curve: TG, dotted curve: DTA.

confirmed until 600 K in the profiles for samples from Group B of the poorly crystalline ZWO-I phase (ZWOH_6M_12h) and the amorphous samples from Group D (ZWOH_0M_12h). This gradual weight loss was attributed to the elimination of the hydroxyl group *via* condensation, including the desorption of adsorbed water. The abrupt weight loss at ~520 K for a highly crystalline phase of ZWOH_6M_48h and ZWOH_10M_12h (Group A) accompanied by a sharp endothermic peak was observed similar to cases for previous studies.[7,8] Assuming that this weight loss up to 873 K corresponded to the transformation of $ZrW_2O_7(OH)_2 \cdot xH_2O$ to ZrW_2O_8, the number of crystal water was estimated to be 2.1 and 2.4. Note that, at >1000 K, broad endothermic phenomena were confirmed for all samples without remarkable weight loss.

3.1.3. Nitrogen adsorption–desorption isotherms. Fig. 3 shows nitrogen adsorption–desorption isotherms of calcined ZWOHs. Moreover, the estimated BET-specific surface area and total pore volume are shown in each figure. Almost all isotherms fit in the type IV category. Fig. S3† summarizes the pore size distribution curves. The pore parameter and surface area were similar when the ZWO-I phase was formed at hydrochloric acid concentrations ranging from 5 to 9 M. The surface area of other samples was less than that of ZWO-I samples.

3.1.4. W L-edge XANES/EXAFS. The characteristic pre-edge peak intensity that appeared in W L1 edge XANES at ~12 100 eV is known to be sensitive to the coordination symmetry of tungsten atom.[43–45] Cubic ZrW_2O_8 (ref. 3 and 4) and In_6WO_{12} (ref. 46) include distorted WO_4 tetrahedron and regular WO_6 octahedron, respectively. Both monoclinic WO_3 and $ZrW_2O_7(OH)_2 \cdot 2H_2O$[6,47] contain distorted WO_6 octahedrons. Fig. 4A shows the W L1 edge XANES spectra of various catalyst samples and reference compounds with different coordination symmetries. The intensity of the pre-edge peak for ZWO-I (ZWOH_6M_12h) and the calcined one was nearly the same as that for highly crystalline $ZrW_2O_7(OH)_2 \cdot 2H_2O$ (ZWOH_6M_48h), WO_3, and conventional tungstated-zirconia catalysts. The apparent absorption edge position of the ZWO-I phase was higher than those of metallic tungsten and $W^{IV}O_2$ and was similar to that of $W^{VI}O_3$ (Fig. 4B).

Fig. 5 shows W L3 edge EXAFS spectra of catalyst samples and their radial structure functions (RSFs) obtained by Fourier transformation. Any distinct peaks were not confirmed at ~3–4 Å in the RSFs of the ZWO-I phases. The calcination procedure at 873 K for the as-synthesized ZWO-I had little effect on the configuration of EXAFS and RSF, whereas calcination at 1073 K resulted in the transformation to nearly the same as those of WO_3 (f). Despite their high crystallinity, certain peaks did not exist in their RSF longer than 2 Å for $ZrW_2O_7(OH)_2 \cdot 2H_2O$ (d), ZrW_2O_8 (e), and WO_3 (f). We are unsure whether we will be able to perform a reliable curve-fitting analysis for the second coordination sphere of the current catalyst system at the W L3 edge. The curve-fitting analysis was then performed only on the first coordination sphere. The results are summarized in Table 1. Single-shell fitting was possible for ZrW_2O_8, whereas two-shell fittings were required for all the other samples. The evaluated EXAFS parameters were not so different from each other except for ZrW_2O_8.
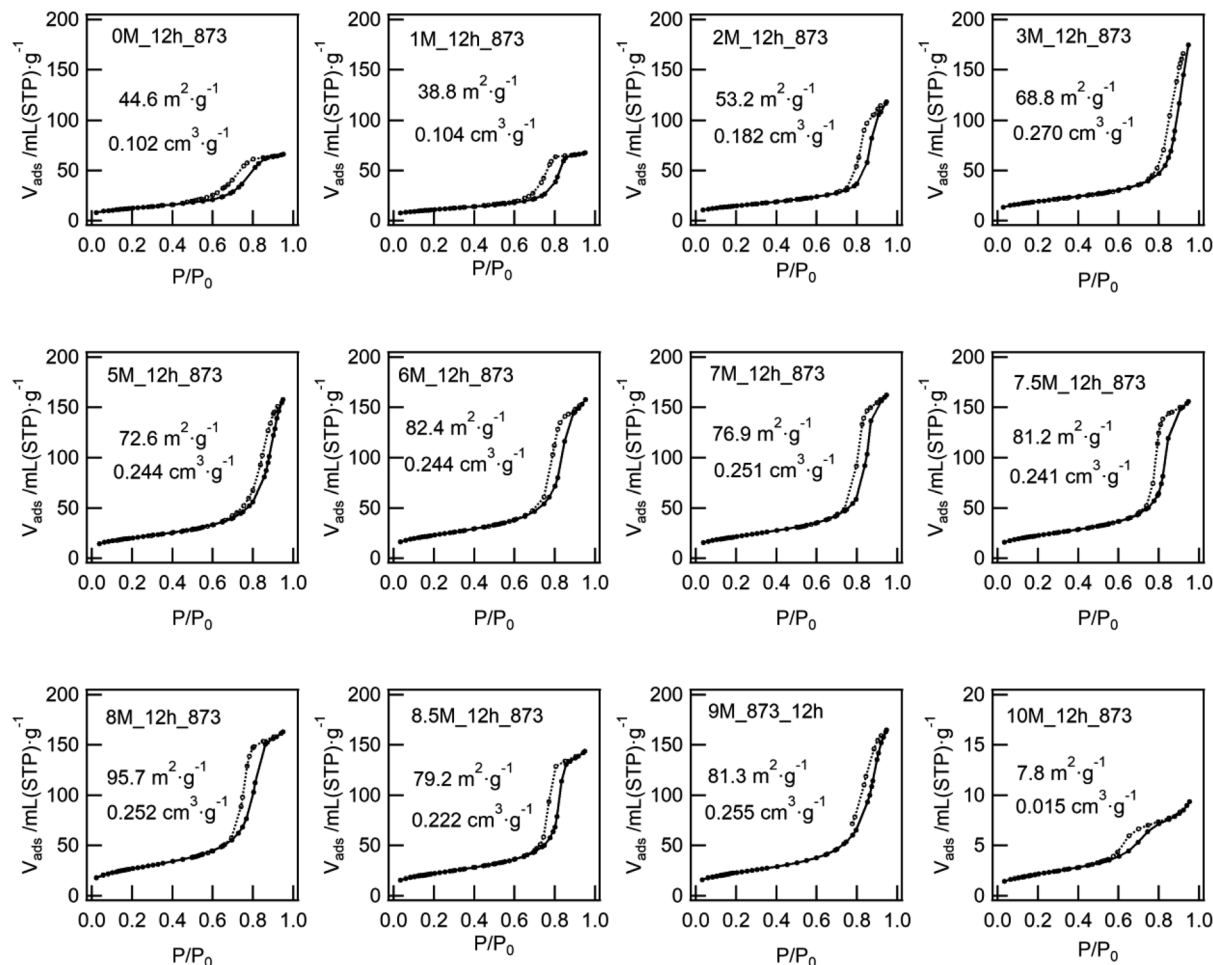
Fig. 3 Nitrogen adsorption/desorption isotherms of calcined binary oxides ZWO_XM_12h_873 prepared with different HCl concentrations (X = 0–10).

3.1.5. Zr-K edge EXAFS. Fig. 6 shows Zr K-edge EXAFS spectra and their RSFs. The RSFs of $ZrW_2O_7(OH)_2$ and ZrW_2O_8 had distinct twin and single peaks for the second coordination
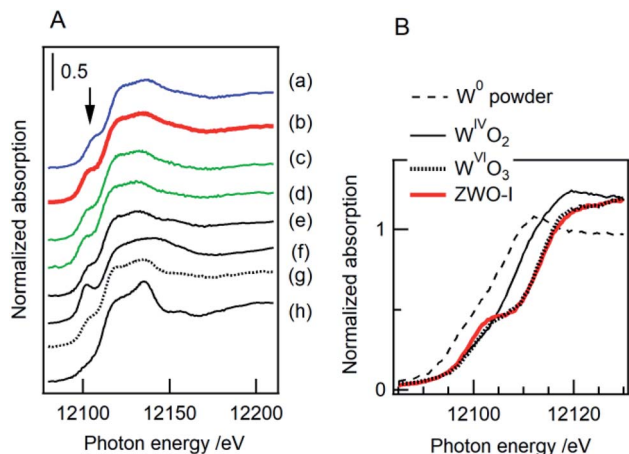

Fig. 4 W L1-edge XANES spectra of (A) the hexavalent tungsten compounds and catalyst samples, and (B) comparison of the absorption edge. (a) ZWOH_6M_12h, (b) ZWO_6M_12h_873 (ZWO-I), (c) tungstated-zirconia (reference), (d) tungstated-zirconia (home-made), (e) $ZrW_2O_7(OH)_2 \cdot 2H_2O$, (f) ZrW_2O_8, (g) WO_3 and (h) In_6WO_{12}.

sphere at ~3.2–3.7 Å and 3.7 Å, respectively. The as-synthesized ZWO-I and calcined one at 873 K (ZWOH_6M_12h, and ZWO_6M_12h_873) possess a small peak at ~3.7 Å as indicated by an arrow. After calcination at 1073 K (ZWO_6M_12h_1073), the configuration of the Zr K-edge EXAFS spectrum and RSF resembled those of monoclinic ZrO_2.

Table 2 summarizes the results of the curve-fitting analysis at the Zr K-edge. In cases for ZWO-I, the small peak at ~3.5 Å in their RSFs is confirmed to be that of the Zr–W pair. The evaluated interatomic distance was comparable to that of the longer one of ZrW_2O_8 and $ZrW_2O_7(OH)_2$. Unlike ZWO-I, the second coordination sphere of the two types of tungstated-zirconia was confirmed to be a Zr–Zr pair. The first coordination sphere at ~1.8 Å could be fitted with a single Zr–O pair for ZrW_2O_8. Two shell fitting was required for all other catalyst samples, but significant differences in EXAFS parameters were not confirmed among them.

3.2. Catalysis

3.2.1. Hydrothermally synthesized binary oxides with ZrW_2O_8 composition. The alkylation of anisole with benzyl alcohol has been recently utilized as one of the useful test reactions of a strong solid acid catalyst.[17,48,49] In this study, we
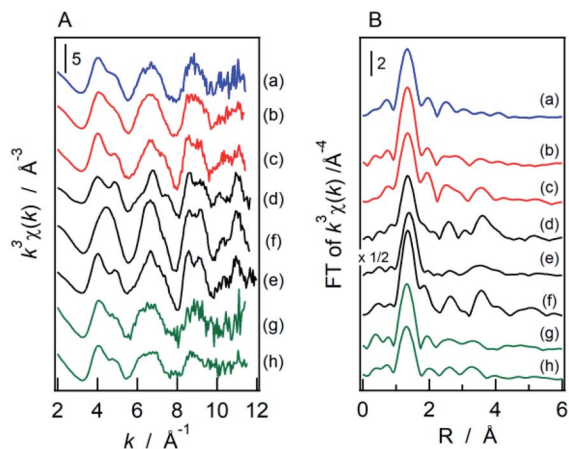
Fig. 5 W L3-edge (A) EXAFS spectra and (B) their Fourier transforms. (a) ZWOH_6M_12h, (b) ZWO_6M_12h_873 (ZWO-I), (c) ZWO_6M_12h_1073, (d) $ZrW_2O_7(OH)_2 \cdot 2H_2O$, (e) ZrW_2O_8, (f) WO_3, (g) tungstated-zirconia (reference), and (h) tungstated-zirconia (home-made).
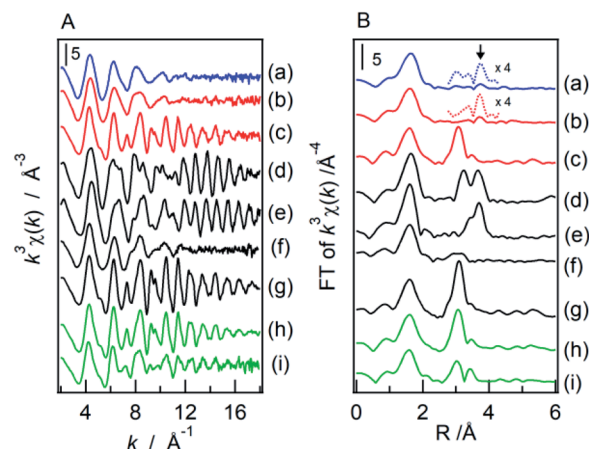

Fig. 6 Zr K-edge (A) EXAFS spectra and (B) their Fourier transforms. (a) ZWOH_6M_12h, (b) ZWO_6M_12h_873 (ZWO-I), (c) ZWO_6M_12h_1073, (d) $ZrW_2O_7(OH)_2 \cdot 2H_2O$, (e) ZrW_2O_8, (f) $Zr(OH)_x$, (g) $m\text{-}ZrO_2$, (h) tungstated-zirconia (reference), and (i) tungstated-zirconia (home-made).

confirmed that a series of ZWO prepared with various HCl concentrations exhibited different catalytic performances that systematically varied. Fig. 7 shows typical results. The selectivity for benzylanisoles and dibenzyl ether was *ca.* 80% and 20%, respectively, for this ZWO catalyst. The reaction rate was evaluated by analyzing the concentration changes of benzyl alcohol with the second-order kinetic model by assuming the volume of the reaction solution was constant. As shown in Fig. S4,† this model was confirmed to be applicable where the conversion was up to *ca.* 40%. Fig. 8 shows the rate constant of benzyl alcohol conversion of the calcined ZWO catalysts plotted as a function of the HCl concentration utilized for catalyst preparation. The BET-specific surface area was indicated in this figure. The activity increased with HCl concentration and reached a maximum at ~6–8 M, and was quite low in the case for the utilized HCl concentration was 10 M. As reported previously,[12] well-crystalline hydroxide

$ZrW_2O_7(OH)_2 \cdot 2H_2O$ (ZWOH_6M_48h) and cubic ZrW_2O_8 (ZWO_6M_48h_873) of the calcined products were inert.

Note that the liquid-phase alkylation of aromatics by solid acid catalysts has been examined using several models such as pseudo-first- or second-order kinetic equation and the Langmuir–Hinshelwood kinetic model.[50] In this study, we confirm that equivalent HCl concentration dependency for the evaluated reaction rate could be obtained in case the pseudo-first-order kinetic equation model is applied.

3.2.2. Reference solid acid catalysts. Finally, the catalytic activity of the ZWO-I phase (ZWOH_6M_12h_873) was compared with other typical solid acids. Fig. 9 shows the rate constant at various reaction temperatures in the range of 363–403 K. The evaluated activation energies were indicated in parentheses, and the value, 124 kJ mol^{-1}, did not differ much among the utilized catalysts. We could confirm that the reaction

Table 1 Results of the curve-fitting analysis of W L3-edge EXAFS

Catalyst	Shell	CN^a	r^b/Å	$\Delta\sigma^c$/Å
ZWOH_6M_12h	W–O	3.31 ± 0.09	1.787 ± 0.011	0.084 ± 0.039
		1.71 ± 1.22	2.111 ± 0.033	0.097 ± 0.109
ZWO_6M_12h_873 (ZWO-I)	W–O	3.30 ± 0.96	1.782 ± 0.012	0.075 ± 0.044
		1.41 ± 1.35	2.098 ± 0.047	0.097 ± 0.152
ZWO_6M_12h_1073	W–O	4.20 ± 1.09	1.793 ± 0.009	0.099 ± 0.036
		1.83 ± 0.91	2.125 ± 0.017	0.060 ± 0.083
$ZrW_2O_7(OH)_2$ (ZWOH_6M_48h)	W–O	2.55 ± 0.64	1.768 ± 0.006	0.076 ± 0.028
		1.78 ± 0.12	2.115 ± 0.022	0.103 ± 0.074
ZrW_2O_8 (ZWO_6M_48h_873)	W–O	3.51 ± 0.56	1.779 ± 0.005	0.053 ± 0.027
WO_3	W–O	3.70 ± 0.84	1.779 ± 0.006	0.080 ± 0.028
		2.12 ± 1.02	2.107 ± 0.016	0.079 ± 0.061
WO_3–ZrO_2 (reference)	W–O	2.86 ± 1.00	1.776 ± 0.020	0.081 ± 0.057
		0.72 ± 1.02	2.053 ± 0.107	0.079 ± 0.261
WO_3–ZrO_2 (home-made)	W–O	3.27 ± 0.96	1.779 ± 0.015	0.105 ± 0.040
		0.90 ± 1.07	2.093 ± 0.072	0.104 ± 0.183

^{a} Coordination number. ^{b} Interatomic distance. ^{c} Debye–Waller factor.

Table 2 Results of the curve-fitting analysis of Zr K-edge EXAFS

Catalyst	Shell	CN^a	r^b/Å	$\Delta\sigma^c$/Å
ZWOH_6M_12h	Zr–O	4.11 ± 4.71	2.113 ± 0.065	$0.082^d \pm 0.065$
		3.15 ± 3.85	2.233 ± 0.073	0.082^d
	Zr–W	1.64 ± 0.16	3.941 ± 0.002	0.092 ± 0.004
ZWO_6M_12h_873 (ZWO-I)	Zr–O	4.05 ± 4.69	2.108 ± 0.070	$0.094^d \pm 0.070$
		3.53 ± 3.69	2.241 ± 0.072	0.094^d
	Zr–W	2.39 ± 0.24	3.943 ± 0.003	0.107 ± 0.005
ZWO_6M_12h_1073	Zr–O	4.75 ± 2.32	2.111 ± 0.027	$0.083^d \pm 0.038$
		3.13 ± 1.49	2.256 ± 0.044	0.083^d
	Zr–Zr	4.06 ± 0.59	3.445 ± 0.003	0.081 ± 0.008
		3.68 ± 2.42	3.977 ± 0.014	0.114 ± 0.039
$ZrW_2O_7(OH_2)_2$ (ZWOH_6M_48h)	Zr–O	3.76 ± 3.19	2.096 ± 0.044	$0.066^d \pm 0.059$
		4.06 ± 2.39	2.214 ± 0.038	0.066^d
	Zr–W	2.67 ± 0.65	3.451 ± 0.004	0.073 ± 0.010
		3.06 ± 0.71	3.910 ± 0.003	0.066 ± 0.010
ZrW_2O_8 (ZWO_6M_48h_873)	Zr–O	6.49 ± 0.88	2.081 ± 0.005	0.079 ± 0.014
	Zr–W	2.86 ± 1.09	3.720 ± 0.007	0.075 ± 0.018
		4.56 ± 1.11	3.900 ± 0.004	0.073 ± 0.011
$Zr(OH)_x$	Zr–O	4.72 ± 2.19	2.121 ± 0.026	$0.080^d \pm 0.036$
		1.89 ± 1.41	2.263 ± 0.050	0.080^d
	Zr–Zr	3.59 ± 1.24	3.390 ± 0.021	0.117 ± 0.023
		0.21 ± 0.49	3.488 ± 0.013	0.063 ± 0.087
m-ZrO_2	Zr–O	4.40 ± 2.23	2.111 ± 0.027	$0.078^d \pm 0.040$
		3.34 ± 1.43	2.252 ± 0.038	0.078^d
	Zr–Zr	4.87 ± 0.68	3.450 ± 0.011	0.075 ± 0.008
		3.80 ± 2.38	3.981 ± 0.013	0.097 ± 0.036
WO_3–ZrO_2 (reference)	Zr–O	5.10 ± 2.67	2.119 ± 0.030	$0.086^d \pm 0.040$
		3.25 ± 1.76	2.265 ± 0.049	0.086^d
	Zr–Zr	4.47 ± 0.67	3.437 ± 0.003	0.083 ± 0.008
		4.82 ± 2.77	3.982 ± 0.013	0.104 ± 0.038
WO_3–ZrO_2 (home-made)	Zr–O	4.99 ± 1.54	2.127 ± 0.017	$0.089^d \pm 0.026$
		2.44 ± 0.85	2.289 ± 0.041	0.089^d
	Zr–Zr	6.61 ± 1.77	3.473 ± 0.013	0.094 ± 0.014
		6.83 ± 2.03	3.644 ± 0.018	0.101 ± 0.021

[a] Coordination number. [b] Interatomic distance. [c] Debye–Waller factor. [d] Constrained to be the same.
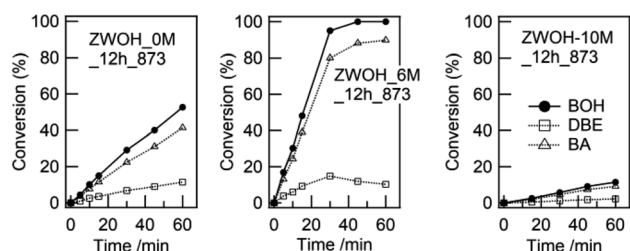

Fig. 7 Typical results of anisole alkylation with benzyl alcohol at 403 K. BOH: benzyl alcohol; DBE: dibenzyl ether; BA: benzyl anisoles.

rate for ZWO-I exhibits almost the same level of catalytic performance as that of the reference catalyst tungstated-zirconia, but was somewhat less than the home-made conventional tungstated- and sulfated-zirconia. The typical strong solid acid amorphous silica promoted this reaction; however, the activity was as low as <1/500 for ZWO-I under the present reaction conditions. Note that mesoporous silica FSM-16 having 2D hexagonally ordered pore structure could promote the reaction as well, however, the activity was less than that of ZWO-I but higher than that of amorphous silica-alumina. As for

Friedel–Crafts type reaction by mesoporous silica, Ishitani *et al.* reported that a series of mesoporous silica MCM-41 promoted the acylation of anisole with carboxylic anhydride, and the catalytic property was originating from the hexagonally ordered pore structure.[51]
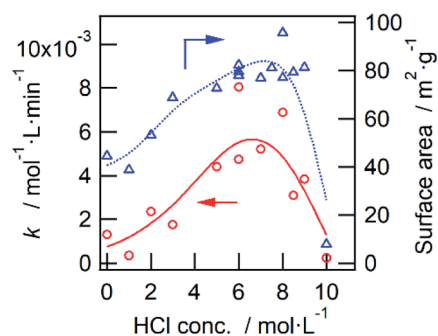

Fig. 8 HCl concentration dependency used for catalyst preparation on the reaction rate for anisole alkylation (circle) and surface area of a catalyst (triangle). Catalyst: ZWO_*X*M_12h_873, 0.1 g; benzyl alcohol: 0.64 mL; anisole: 10 mL; and reaction temperature: 403 K.
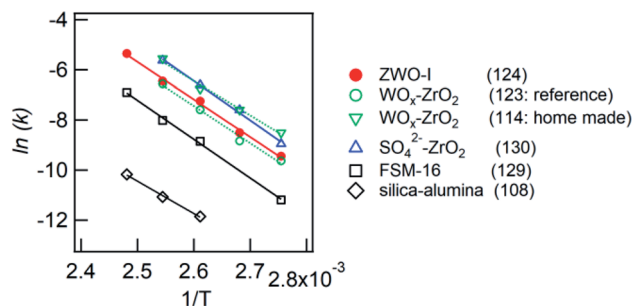
Fig. 9 Arrhenius plot for anisole alkylation with benzyl alcohol. Catalyst: 0.1 g; benzyl alcohol: 0.64 mL; anisole: 10 mL. Values in parentheses show the activation energy (kJ mol^{-1}).

4. Discussion

4.1. Formation of poorly crystalline binary hydroxide ZWO-I phase

In this study, we confirmed that the poorly crystalline ZWO-I phase formed by the hydrothermal treatment of a mother gel for 12 h when 4–9 M HCl was added in their preparation. It has been reported that halide and hydronium ion concentrations are related to the reaction rate of crystallization and/or nucleation of a precursor of zirconium tungstate hydroxide.[8,27] The present XRD patterns of the as-synthesized binary hydroxide with different hydrothermal treatment times (Fig. S1†) show that the ZWO-I phase is one of the metastable phases. A longer hydrothermal treatment would result in the transformation to a more stable $ZrW_2O_7(OH)_2 \cdot 2H_2O$. This crystallization might occur until 12 h in the case 10 M HCl was used, as described in 3.1.1. ZWO-I phase was not formed even after 72 h of hydrothermal treatment at 453 K in case HCl concentration was <1 M. Then, we conclude that 6 M HCl is the best for forming the ZWO-I phase under this 12 h hydrothermal treatment at 453 K. The endothermic phenomena above 1000 K without weight loss were confirmed for all TG-DTA profiles. These phenomena were possibly attributed to the decomposition of a binary phase to WO_3 and ZrO_2. The similarity of the W L3 edge or Zr K-edge EXAFS spectra of ZWO_XM_1073 to the crystalline WO_3 and ZrO_2 supports this deduction.

4.2. Active species

We confirmed that the calcined ZWO-I phase (ZWO_XM_873: Group B, X: 5–8) exhibited high activity for the anisole alkylation with benzyl alcohol. Calcined Group C and D catalysts (X: 0–3) promoted this reaction; however, the activities were lower than those of Group B. Although the ZWO-I phase was not confirmed in the XRD patterns of Group D (X: 0, 1), alkylation was promoted to some extent. This shows X-ray amorphous zirconium–tungsten binary oxides possess solid acidity, and the intrinsic activity is lower than that of the ZWO-I phase itself. Consequently, the highest activity per catalyst weight was achieved in cases where utilized HCl concentration for the catalyst preparation was 5–8 M. A series of Group-B ZWO-I catalysts (ZWO_XM_873, X = 5–9) have the equivalent level of surface

area (80 $\pm$ 6 m^2 g^{-1}, n = 9). The surface area of Group A (ZWO_10M_873) was 8 m^2 g^{-1}, whereas highly crystalline $ZrW_2O_7(OH)_2 \cdot 2H_2O$ (ZWOH_6M_48–240h, ZWOH_10M_12h) and calcined ones (cubic ZrW_2O_8) were as small as ca. 1–2 m^2 g^{-1}. This suggests that a small number of poorly crystalline ZWO-I phase coexists accompanied by crystalline ZrW_2O_8 phase, and then alkylation was slightly promoted.

As described in the Introduction section, XRD patterns similar to this ZWO-I phase have been reported by many research groups.[27,28] Ando *et al.* reported that the calcined binary oxides (W/Zr = 1.4) at 673 K promoted the alkylation of anisole with benzyl alcohol. We believe that their catalysts are fundamentally similar to the present ZWO-I samples. Because no sulfate salts or sulfuric acid was used during our catalyst preparation procedure, we conclude this ZWO-I phase acts as a strong solid acid. The catalytic performance is suggested to be the same level as that of reference tungstated-zirconia.

The initial benzyl anisole production rate per ZWO-I weight was the same in cases where the catalyst amount was reduced to 1/10, as shown in Fig. S5.† The higher yield per ZWO-I weight was obtained at the higher substrate/catalyst ratio. It has been reported that the initial rate for the alkylation of toluene by benzyl alcohol over ion-exchanged clays exhibited roughly correlate with a number of Brønsted acid sites.[52] We presume that the alkylation of anisole with benzyl alcohol is promoted by Brønsted acid sites on ZWO-I, as in a typical Friedel–Crafts reaction. This catalyst amount dependency suggests that the activation of benzyl alcohol by ZWO-I would control the reaction rate.

4.3. Structure of ZWO-I phase

As shown in the W L1 edge XANES spectra (Fig. 4), the pre-edge peak intensities of ZWO-I samples (ZWOH_6M_12h_as, ZWOH_6M_12h_873) were almost similar to those of $ZrW_2O_7(OH)_2$ and WO_3, which contain distorted WO_6 units. The characteristic pre-edge peak intensity in W L1 edge XANES is well known to be sensitive to the coordination geometry.[43–45] The similarity of the pre-edge peak intensity and the apparent absorption edge energy position suggest tungsten species in ZWO-I are distorted octahedral $W^{VI}O_6$.

The RSFs of the ZWO-I phase at Zr K edge EXAFS afforded a single tiny peak, while distinct twin peaks could be observed in the RSF of ZrW_2O_8 and $ZrW_2O_7(OH)_2$. Crystallographic data for ZrW_2O_8 (ref. 3 and 53) and $ZrW_2O_7(OH)_2$ (ref. 6 and 47) show that two types of Zr–(O)–W pairs exist with different bond lengths. The shorter and longer bond lengths correspond to edge-sharing and corner-sharing Zr–O–W linkage between ZrO_n and WO_n polyhedron. The Zr–O–W bond length evaluated for ZWO-I phase samples was similar to the longer ones of the corner-sharing units. The EXAFS parameters of Zr–O pairs were similar to those for $ZrW_2O_7(OH)_2$ and monoclinic ZrO_2; the Zr–O polyhedron present in the two compounds is ZrO_7. Distinct peaks at ~2–4 Å were not confirmed in RSFs of ZWO-I samples and conventional tungstated-zirconia at the W L3 edge. We presume that the Zr–(O)–W linkage exists in the ZWO-I phase, but the narrow available k-ranges of W L3-edge EXAFS and/or

the large Debye–Waller factor because of structural disorder might make it difficult to obtain their structural information. Unfortunately, we could not identify additional clear evidence around the local structure of W species in ZWO-I. Based on W L-edge and Zr K-edge XANES/EXAFS characterization, we propose that the Zr species in ZWO-I comprises ZrO_7 polyhedron and distorted WO_6 octahedron, each of which connects *via* a corner-sharing linkage. The ZWO-I phase was formed during the hydrothermal treatment of the mother gel before crystallization to $ZrW_2O_7(OH)_2$. We considered that ZWO-I is a metastable phase having a local structure similar to $ZrW_2O_7(OH)_2$, while the periodic structural network is incomplete where the edge-sharing polyhedral linkage is missing. The longer hydrothermal treatment would result in the formation of edge-sharing polyhedral units, leading to crystallization to $ZrW_2O_7(OH)_2$. Moreover, the evaluated coordination number for the Zr–(O)–W pair of ZWO-I was slightly smaller than that of the longer one of highly crystalline $ZrW_2O_7(OH)_2$.

We propose that only corner-sharing ZrO_7–WO_6 connections exist in the ZWO-I phase, and the incompleteness of the network would be responsible for generating strong acidity. The XRD pattern of the ZWO-I phase was not changed after the catalytic test at 363 K. Note that EXAFS characterization of an-synthesized and calcined ZWO-I samples demonstrated no discernible structural differences at the Zr K- and W L-edges. The calcination procedure significantly altered the pore structure and surface area (Fig. S6†). The activity enhancement behavior on calcination is a subject for additional investigation.

5. Conclusions

Hydrothermally synthesized poorly crystalline metastable Zr–W binary oxides (W/Zr = 2) act as strong solid acids to promote the anisole alkylation with benzyl alcohol. The catalytic performance was comparable to that of the reference conventional tungstated-zirconia. The HCl concentration used to prepare a mother gel controlled the crystalline phase (ZWO-I). The catalytically active phase was obtained in cases where HCl concentration was 5–8 M, and the hydrothermal treatment was performed at 453 K for 12 h. A higher HCl concentration and/or a longer hydrothermal treatment afforded a catalytically inert, highly crystalline $ZrW_2O_7(OH)_2 \cdot 2H_2O$. The W species in ZWO-I existed as a six-valent WO_6 distorted octahedron connected to the ZrO_7 unit *via* corner-sharing linkage. The local structure was suggested to resemble that of $ZrW_2O_7(OH)_2$, although edge-sharing Zr–O–W linkage was missing. The incompleteness of the network structure would be responsible for the strong solid acidity.

Author contributions

Takashi Yamamoto: conceptualization, investigation, writing. Seina Heiuchi: investigation. Maki Kondo: investigation. Kei Tabusadani: validation. Atsushi Sakaki: synchrotron XAFS experiment.

Conflicts of interest

There are no conflicts to declare.

Acknowledgements

References

1 L. L. Y. Chang, M. G. Scroger and B. Phillips, *J. Am. Ceram. Soc.*, 1967, **50**, 211–215.
2 C. Martinek and F. A. Hummel, *J. Am. Ceram. Soc.*, 1968, **51**, 227–228.
3 J. S. O. Evans, T. A. Mary, T. Vogt, M. A. Subramanian and A. W. Sleight, *Chem. Mater.*, 1996, **8**, 2809–2823.
4 T. A. Mary, J. S. O. Evans, T. Vogt and A. W. Sleight, *Science*, 1996, **272**, 90–92.
5 C. Closmann, A. W. Sleight and J. C. Haygarth, *J. Solid State Chem.*, 1998, **139**, 424–426.
6 M. S. Dadachov and R. M. Lambrecht, *J. Mater. Chem.*, 1997, **7**, 1867–1870.
7 Q. F. Xing, X. R. Xing, R. B. Yu, L. Du, J. Meng, J. Luo, D. Wang and G. R. Liu, *J. Cryst. Growth*, 2005, **283**, 208–214.
8 J. A. Colin, D. V. Camper, S. D. Gates, M. D. Simon, K. L. Witker and C. Lind, *J. Solid State Chem.*, 2007, **180**, 3504–3509.
9 L. C. Kozy, M. N. Tahir, C. Lind and W. Tremel, *J. Mater. Chem.*, 2009, **19**, 2760–2765.
10 H. Wu, P. Badrinarayanan and M. R. Kessler, *J. Am. Ceram. Soc.*, 2012, **95**, 3643–3650.
11 A. I. Gubanov, E. S. Dedova, P. E. Plyusnin, E. Y. Filatov, T. Y. Kardash, S. V. Korenev and S. N. Kulkov, *Thermochim. Acta*, 2014, **597**, 19–26.
12 T. Yamamoto, M. Kondo, T. Irie and N. Tanima, *Adv. X-Ray Chem. Anal., Jpn.*, 2017, **48**, 137–148.
13 K. Arata and M. Hino, *Proc. 9th Int. Congr. Catal.*, 1988, pp. 1727–1734.
14 M. Hino and K. Arata, *J. Chem. Soc., Chem. Commun.*, 1988, 1259–1260.
15 A. Corma, *Chem. Rev.*, 1995, **95**, 559–614.
16 K. Arata, *Appl. Catal., A*, 1996, **146**, 3–32.
17 H. Hattori and Y. Ono, *Solid Acid Catalysis*, Pan Stanford, Singapore, 2015.
18 W. Zhang, Z. Wang, J. Huang and Y. Jiang, *Energy Fuels*, 2021, **35**, 9209–9227.
19 M. Scheithauer, R. K. Grasselli and H. Knözinger, *Langmuir*, 1998, **14**, 3019–3029.
20 D. G. Barton, M. Shtein, R. D. Wilson, S. L. Soled and E. Iglesia, *J. Phys. Chem. B*, 1999, **103**, 630–640.

21 N. Naito, N. Katada and M. Niwa, *J. Phys. Chem. B*, 1999, **103**, 7206–7213.

22 T. Yamamoto, A. Orita and T. Tanaka, *X-Ray Spectrom.*, 2008, **37**, 226–231.

23 W. Zhou, E. I. Ross-Medgaarden, W. V. Knowles, M. S. Wong, I. E. Wachs and C. J. Kiely, *Nat. Chem.*, 2009, **1**, 722–728.

24 C. Thomas, *J. Phys. Chem. C*, 2011, **115**, 2253–2256.

25 T. Yamamoto, A. Teramachi, A. Orita, A. Kurimoto, T. Motoi and T. Tanaka, *J. Phys. Chem. C*, 2016, **120**, 19705–19713.

26 W. Zhou, N. Soultanidis, H. Xu, M. S. Wong, M. Neurock, C. J. Kiely and I. E. Wachs, *ACS Catal.*, 2017, **7**, 2181–2198.

27 X. R. Xing, Q. F. Xing, R. B. Yu, J. Meng, J. Chen and G. R. Liu, *Phys. B*, 2006, **371**, 81–84.

28 M. Ando, A. Izumi, T. Murayama and W. Ueda, *Abst. 108th CATSJ (Catalysis Society of Japan) Meetings*, 2011, p. 1F11.

29 M. Lucas, K. Fabičovicová and P. Claus, *ChemCatChem*, 2018, **10**, 612–618.

30 M. Hino, S. Kobayashi and K. Arata, *J. Am. Chem. Soc.*, 1979, **101**, 6439–6441.

31 X. Song and A. Sayari, *Catal. Rev.*, 1996, **38**, 329–412.

32 S. Inagaki, Y. Fukushima and K. Kuroda, *J. Chem. Soc., Chem. Commun.*, 1993, 680–682.

33 T. Yamamoto, T. Tanaka, T. Funabiki and S. Yoshida, *J. Phys. Chem. B*, 1998, **102**, 5830–5839.

34 T. Yamamoto, T. Tanaka, S. Inagaki, T. Funabiki and S. Yoshida, *J. Phys. Chem. B*, 1999, **103**, 6450–6456.

35 T. Yamamoto, S. Mori, T. Shishido, J. Kawai and T. Tanaka, *Top. Catal.*, 2009, **52**, 657–663.

36 T. Taguchi, J. Harada, A. Kiku, K. Tohji and K. Shinoda, *J. Synchrotron Radiat.*, 2001, **8**, 363–365.

37 T. Yamamoto, S. Mori, T. Kawaguchi, T. Tanaka, K. Nakanishi, T. Ohta and J. Kawai, *J. Phys. Chem. C*, 2008, **112**, 328–331.

38 T. Taguchi, T. Ozawa and H. Yashiro, *Phys. Scr.*, 2005, **T115**, 205–206.

39 A. L. Ankudinov, B. Ravel, J. J. Rehr and S. D. Conradson, *Phys. Rev. B: Condens. Matter Mater. Phys.*, 1998, **58**, 7565–7576.

40 L. Bartha, A. B. Kiss and T. Szalay, *Int. J. Refract. Met. Hard Mater.*, 1995, **13**, 77–91.

41 G. Liu, S. Wang, Y. Nie, X. Sun, Y. Zhang and Y. Tang, *J. Mater. Chem. A*, 2013, **1**, 10120–10129.

42 P. Ou, X. Su, Y. Zeng, F. Zhang, J. Liu, C. Wang, S. Yang, H. Wang, Y. Wen and H. Zhao, *CrystEngComm*, 2021, **23**, 1700–1703.

43 J. A. Horsley, I. E. Wachs, J. M. Brown, G. H. Via and F. D. Hardcastle, *J. Phys. Chem.*, 1987, **91**, 4014–4020.

44 T. Yamamoto, *X-Ray Spectrom.*, 2008, **37**, 572–584.

45 S. Yamazoe, Y. Hitomi, T. Shishido and T. Tanaka, *J. Phys. Chem. C*, 2008, **112**, 6869–6879.

46 D. Michel and A. Kahn, *Acta Crystallogr., Sect. B: Struct. Crystallogr. Cryst. Chem.*, 1982, **38**, 1437–1441.

47 Y. Cao, X. Deng, H. Ma, S. Wang and X. Zhao, *Defect Diffus. Forum*, 2006, **251–252**, 21–26.

48 K. Okumura, K. Yamashita, M. Hirano and M. Niwa, *J. Catal.*, 2005, **234**, 300–307.

49 A. Takagaki, D. Lu, J. N. Kondo, M. Hara, S. Hayashi and K. Domen, *Chem. Mater.*, 2005, **17**, 2487–2489.

50 P. Beltrame and G. Zuretti, *Green Chem.*, 2004, **6**, 7–13.

51 H. Ishitani, H. Naito and M. Iwamoto, *Catal. Lett.*, 2008, **120**, 14–18.

52 T. Cseri, S. Békássy, F. Figueras and S. Rizner, *J. Mol. Catal. A: Chem.*, 1995, **98**, 101–107.

53 F. D. Vila, J. W. Spencer, J. J. Kas, J. J. Rehr and F. Bridges, *Front. Chem.*, 2018, **6**, 356.